Assessment of the compositional requirements to form Fe-Mn-C austenite-martensite composites

Marcel Muench[a], Reza Gholizadeh[b], Nobuhiro Tsuji[b], Martin Peterlechner[c], Yolita M. Eggeler[c], Jan L. Riedel[a], Michael K. Eusterholz[a,d], Martin Heilmaier[a] and Alexander Kauffmann[*a]

[a] Institute for Applied Materials (IAM-WK), Karlsruhe Institute of Technology (KIT), Kaiserstraße 12, 76131 Karlsruhe, Germany

[b] Department of Materials Science and Engineering, Kyoto University, Sakyo-kyu, Kyoto 606-8501, Japan

[c] Laboratory for Electron Microscopy (LEM), Karlsruhe Institute of Technology (KIT), Engesserstr. 7, 76131 Karlsruhe, Germany

[d] Karlsruhe Nano Micro Facility (KNMFi), Karlsruhe Institute of Technology (KIT), Hermann-von-Helmholtz-Platz 1, 76344 Eggenstein-Leopoldshafen, Germany

* corresponding author
mail: alexander.kauffmann@kit.edu (A. Kauffmann)
phone: +49 721 608 42346

Abstract

Recently, a new generation of high strength steels was introduced by using a lateral chemical pattern of an austenite stabilizer before quenching from partially homogenized austenite to succeed with fine-scaled microstructures of austenite and martensite. A pearlitic microstructure of ternary Fe-Mn-C is a suitable initial state for this when Mn effectively partitions into the cementite. In the present study, two model Fe-Mn-C alloys were first pearlite treated outside the well-established local equilibrium (LE), Mn partitioning (P-LE) and negligible-partitioning (NP-LE) regimes and subsequently underwent a short-time austenitization with the aim of achieving a completely austenitic-martensitic microstructure while retaining the morphology of the initial pearlite. A pearlite formation was achieved not only for Fe-3.0Mn-3.0C (at.%, Alloy A) at high pearlite formation temperature but also for Fe-6.9Mn-3.2C (at.%, Alloy B) at low transformation temperature. The morphology of the pearlite included fibers as well as lamellae, with Alloy A being mostly fibrous. Even though outside the P-LE (and NP-LE) region, a significant Mn partitioning into the cementite was obtained for both alloys. In both cases, pearlite was formed inheriting approximately the overall Mn content, while growing either enriched or depleted in C for most of the reaction. The Mn pattern in both alloys was sufficient to achieve an entirely austenitic-martensitic microstructure with mostly retained morphology from the initial pearlite. Thus, novel fine-structured, austenitic-martensitic composites can be synthesized well outside the previously established Mn partitioning regimes, enabling a large variation of compositions as well as heat treatment parameters.

Keywords

Pearlite, Austenite, Martensite, Fe-Mn-C, Transformation

1 Introduction

1   In 2018, Sun et al. [1] introduced a promising processing route to achieve an outstanding combination
2   of strength and ductility in Mn containing steels by fine-scaled austenite-martensite microstructures.
3   The basic premise is to form a chemical Mn pattern in austenite γ-(Fe,Mn,C) prior to quenching. The
4   Mn pattern gets introduced via an initial pearlite formation, where Mn is strongly enriched in the
5   cementite θ-(Fe,Mn)$_3$C compared to the ferrite α-(Fe,Mn,C). In a subsequent short-time austenitization
6   (STA) treatment, this pattern remains stable under suitable processing conditions, even after the
7   complete transformation to austenite γ-(Fe,Mn,C). Rapid cooling after the completion of the austenite
8   transformation results in a microstructure similar in morphology and dimensions to the initial pearlite,
9   consisting of martensite (Mn depleted regions) and metastable austenite (Mn enriched regions). By
10   additional tempering treatments, remarkable ultimate tensile strength and strain to failure combinations
11   of 1.6-2.1 GPa and 7-10 % were achieved [1].

12   These results were achieved with a hypo-eutectoid alloy composition of Fe-4.3Mn-2.3C (at.%, Fe-
13   4.4Mn-0.5C in wt.%) [1]. In order to test the limits of this scheme, one obvious possibility would be the
14   manipulation of the alloy composition. As the final microstructure and therefore also the resulting
15   mechanical properties strongly depend on the Mn pattern, a variation of the overall Mn content would
16   be a feasible objective. However, the recent endeavors on this topic [1–5], including the original work,
17   strictly focus on Mn contents in a range of only 2-5 at.% Mn and a C content that results in an overall
18   hypo-eutectoid composition. This narrow compositional range might be rationalized by what was
19   suggested in the early work of Hutchinson et al. [6] on the growth kinetics and local equilibrium (LE)
20   conditions of Fe-Mn-C pearlite. Their work introduces two separate design principles for pearlite
21   transformed inside the three-phase field of α-(Fe,Mn,C) + θ-(Fe,Mn)$_3$C + γ-(Fe,Mn,C) as well as in the
22   two-phase field with only α-(Fe,Mn,C) + θ-(Fe,Mn)$_3$C to predict the LE at the reaction front.

23   For the alloy design in Ref. [6], two partitioning boundaries for a given temperature were constructed
24   to obtain the Mn partitioning to α-(Fe,Mn,C) and θ-(Fe,Mn)$_3$C (in the two-phase field), both of which
25   were anticipated to be decisive to succeed in the processing scheme. These boundaries originate from
26   LE design principles on pro-eutectoid α-(Fe,Mn,C) and θ-(Fe,Mn)$_3$C formation and the vastly different
27   diffusion coefficients of interstitial, fast-diffusing C compared to substitutional, slow-diffusing Mn,
28   having a diffusivity ratio of about $10^4 – 10^6$ [7]. These fundamentals have previously been applied
29   qualitatively to pearlite formation by Coates and Hillert [7, 8]. Illustrated in an isothermal section of the
30   ternary phase diagram, two major regimes were derived: (i) a partitioning regime (P-LE) where the Mn
31   partitioning criteria are fulfilled for *both* phases and (ii) a negligible-partitioning regime (NP-LE) where
32   the criteria are *not* satisfied for either of the two. As the pearlite formation with a sufficiently strong Mn
33   partitioning is a prerequisite for the aforementioned novel processing route, the introduction of these
34   regimes heavily restricts the applicable range of alloy compositions and transformation temperatures, as
35   staying inside the P-LE regime seemed reasonable [6].

36   However, what has not been experimentally addressed in literature thus far is the existence of an
37   additional third and fourth regime besides P-LE and NP-LE. In these regimes, only one of the two
38   partitioning criteria is fulfilled, either for α-(Fe,Mn,C) or θ-(Fe,Mn)$_3$C, respectively. The regime of
39   interest for this work is the one that fulfills the Mn partitioning criterion for α-(Fe,Mn,C), but not for
40   θ-(Fe,Mn)$_3$C. With respect to the pearlite formation, Mn exhibits a low equilibrium solubility in
41   α-(Fe,Mn,C) similar to C. This regime includes a large range of temperatures and compositions,
42   especially at higher Mn and C contents, which have yet to be applied for this processing scheme.
43   However, with increasing Mn content the eutectoid line as well as the three-phase field that separates

44 the γ-(Fe,Mn,C) single-phase field and the α-(Fe,Mn,C) + θ-(Fe,Mn)$_3$C two-phase field, shift to lower
45 temperatures [9]. A lower transformation temperature as well as high contents of the slow-diffusing Mn
46 will result in a currently unknown retardation of the pearlite transformation. Another aspect that needs
47 to be considered at such retarded reaction velocities is the formation of metastable phases or other
48 microstructures than α-(Fe,Mn,C) + θ-(Fe,Mn)$_3$C pearlite. In case of Fe-Mn-C, potential formation of
49 M$_5$C$_2$ [10] and M$_{23}$C$_6$ carbides needs to be considered, with M representing metallic elements. Their
50 formation has been reported for example in Cr-rich and Al-rich, Mn-containing steels [10, 11].

51 Thus, the following research questions will be addressed in the present study:

1. Does a pearlite treatment for a low Mn containing Fe-3.0Mn-3.0C (at.%) at 600 °C and for a
   high Mn containing Fe-6.9Mn-3.2C (at.%) at 540 °C result in an entirely transformed
   microstructure comprising pearlite that only consists of α-(Fe,Mn,C) and θ-(Fe,Mn)$_3$C?
2. Does pearlite in these Fe-Mn-C alloys, formed with a set of parameters outside the proposed P-
   LE and NP-LE regimes, exhibit considerable Mn partitioning and how does it compare to global
   equilibrium (GE) and local equilibrium (LE) conditions?
3. Is it possible to achieve an austenitic-martensitic microstructure by short-time austenitization
   from these pearlite conditions?

2 Experiments and Simulations

60 The design of the Mn partitioning boundaries was first developed for pro-eutectoid ferrite and cementite
61 formation [7, 12] and quantitatively applied to Fe-Mn-C pearlite formation by Hutchinson et al. [6].
62 Their application for given isothermal sections is shown in Fig. 1. It divides the parameter space,
63 described by X_C and X_{Mn} as the molar fraction of C and Mn, respectively into four regions. The
64 representation in Fig. 1 is, however present by using the derived quantities $U_C = X_C/(1 - X_C)$ and
65 $U_{Mn} = X_{Mn}/(1 - X_C)$ according to the treatment by Hillert [8, 12] as well as Coates [7] and
66 Hutchinson [6]. A detailed explanation of the physical meaning and practical usage of these variables
67 can be found in the Supplementary Material of this article. The temperatures of 600 (Fig. 1 a)) and
68 540 °C (Fig. 1 b)) were selected to capture a potentially fast transformation at low Mn contents and a
69 retarded one at high Mn contents, respectively. The design of the partitioning boundaries (dot-dashed,
70 purple lines in Fig. 1) are adopted from Ref. [7] and comprehensively described for the present cases in
71 the Supplementary Material, Fig. S1. The thermodynamic data was obtained using the 2024 PanHEA
72 database in the Pandat software provided by CompuTherm (USA). The theoretical data on the phase
73 field positions of the Fe-Mn-C system are in good agreement with experimental literature data in the
74 relevant compositional range [1, 9, 13–21]. All additional thermodynamic LE considerations that are
75 not captured by Pandat were obtained using self-developed Matlab scripts which are published public
76 domain [22].

77 Out of these four regimes formed from the two partitioning boundaries, only two have been addressed
78 in literature thus far [6–8]: The P-LE regime (highlighted in purple), where Mn partitioning is
79 thermodynamically necessary and the NP-LE regime (highlighted in gray), where negligible partitioning
80 may occur. For the pearlite transformation, the two regimes are uniquely defined via the fulfillment of
81 the two independent Mn partitioning criteria for α-(Fe,Mn,C) and θ-(Fe,Mn)$_3$C formation (see
82 Supplementary Material Fig. S1).

83 Two regimes exist with only one of the partitioning criteria being fulfilled and situated at higher as well
84 as lower U_C and U_{Mn}. As it contains a much larger range of $U_C - U_{Mn}$ combinations, the regime to the
85 right of the intersection of the two dot-dashed purple lines in Figs. 1 a) and b) is the scope of the present

86 article. It includes high overall Mn contents which hold the potential of stabilizing large fractions of
87 metastable γ-(Fe,Mn,C) in the final microstructure after STA. Here, the partitioning criteria are fulfilled
88 for α-(Fe,Mn,C), but not for θ-(Fe,Mn)$_3$C formation.

89 Inside this regime two model alloys, Alloy A and Alloy B, were selected. They lie inside the
90 α-(Fe,Mn,C) + θ-(Fe,Mn)$_3$C two-phase field as well as inside the metastable extensions of the
91 α-(Fe,Mn,C) + γ-(Fe,Mn,C) and γ-(Fe,Mn,C) + θ-(Fe,Mn)$_3$C phase field boundaries to avoid pro-
92 eutectoid ferrite or cementite formation. The nominal compositions of the Mn-lean Alloy A and the Mn-
93 rich Alloy B are Fe-3.0Mn-3.0C and Fe-6.9Mn-3.2C (at.%, Fe-3.0Mn-0.7C and Fe-7.0Mn-0.7C in
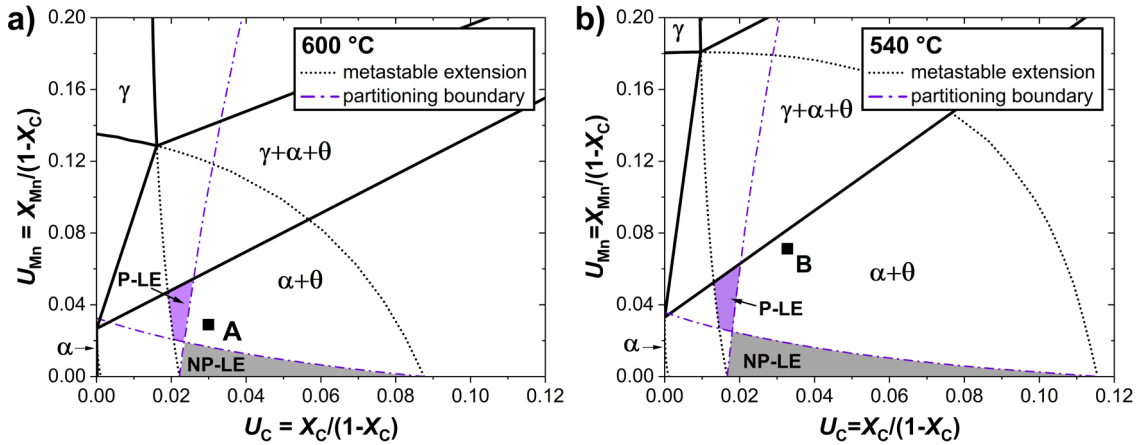94 wt.%), respectively.

Fig. 1: Fe-Mn-C isothermal sections at a) 600 °C and b) 540 °C. Black bold lines illustrate the phase fields in global equilibrium. Black dotted lines indicate the metastable extrapolations of the α-(Fe,Mn,C) + γ-(Fe,Mn,C) and γ-(Fe,Mn,C) + θ-(Fe,Mn)$_3$C phase field boundaries. The purple dot-dashed lines represent Mn partitioning boundaries for α-(Fe,Mn,C) (near horizontal) and θ-(Fe,Mn)$_3$C (near vertical). P-LE and NP-LE regions are marked purple and gray, respectively. Alloys A and B, both lie outside these regions.

95 Alloy manufacturing was done by arc melting high purity bulk elements as well as an in-house
96 synthesized Fe$_3$C obtained by the same method. The elements Mn (etched nominal purity 99.8 %) and
97 graphite (nominal purity 99.999 %) were provided by chemPUR GmbH (Germany). Fe (nominal purity
98 99.99 %) was provided by Alfa Aesar (United States). Arc melting was conducted in an AM/0.5 furnace
99 provided by Edmund Bühler GmbH (Germany). The furnace chamber was evacuated to $5 \cdot 10^{-2}$ mbar
100 and filled with Ar. This process was repeated for three times in total in order to purify the melting
101 atmosphere. Then, a vacuum of less than $1 \cdot 10^{-4}$ mbar was established. The processing chamber was
102 then filled with Ar once more to a pressure of 600 mbar. Residual O$_2$ within the furnace chamber was
103 gettered by liquefying a Zr granule before melting the bulk elements. Every manufactured ingot was
104 flipped and re-melted at least five times. The alloy ingots were homogenized utilizing a STF15/450 21-
105 601449 tube furnace by Carbolite Gero GmbH & Co. KG (Germany) with flowing high purity Ar
106 atmosphere. The heat treatment temperature was 1100 °C for a dwell time of 96 h. Heating and cooling
107 were conducted at a rate of 115 K/h. The chemical composition was determined through optical emission
108 spectroscopy (OES) by analyzing both, the top and bottom side after the last re-melting step. The results
109 can be seen in Tab. 1. The standard deviation for all elements was determined to be < 0.07 at.%
110 (0.07 wt.%). Samples for further investigations were cut from the alloy batches by the use of a high-
111 speed rotary cutting device (Struers, France).

112 Pearlite formation was carried out in air at atmospheric pressure using two pre-heated box furnaces.
113 After completion of the prior austenitization step at 910 °C for 1 h, an immediate furnace transfer was
114 performed. Pearlite in Alloy A and Alloy B was formed at 600 °C for 16 h and 540 °C for 96 h,

115 respectively, based on initial trials to obtain relevant temperature/time combinations. The heat
116 treatments were concluded by oil quenching.

117 The STA treatments were done in a pre-heated box furnace at 770 °C for 150 s and also concluded by
118 oil quenching. To ensure a high heating rate, the samples were covered by pre-heated Al_2O_3 powder at
119 the start of the treatment.

120 The samples for microstructure characterization were prepared by water-cooled grinding with SiC paper
121 followed by standard metallographic polishing steps with 3 and 1 μm polycrystalline diamond
122 suspensions. As a finishing step, polishing with MasterMet-2 by Buehler (USA) was performed for
123 5 min. Samples were subsequently etched in a 1 % Nital solution for 5 s. The grinding process was
124 carried out to remove any decarburized layer that has formed during the heat treatments. Microstructure
125 characterization was performed by scanning electron microscopy (SEM). For secondary electron (SEM-
126 SE) as well as backscattered electron (SEM-BSE) contrast imaging, a Leo Gemini 1530 field-emission
127 SEM by Zeiss (Germany) was utilized. The quantification of the dimensions of microstructural details
128 was carried out using ImageJ software. Phase identification was done via selected area electron
129 diffraction (TEM-SAED) with a JEM-2100F by Jeol (Japan) and a Titan3 by FEI (USA) transmission
130 electron microscope (TEM) operated at 200 kV and 300 kV, respectively. In order to obtain the chemical
131 composition of all phases formed with respect to Fe, Mn and C, atom probe tomography (APT)
132 experiments were performed on both alloys after pearlite formation with a LEAP 4000X HR by Cameca
133 (France). All of the presented data were generated from evaporation in voltage mode. Tip preparation
134 was done via focused ion beam (FIB) milling with an Auriga 60 by Zeiss (Germany). Peak
135 decomposition was required for the θ-$(Fe,Mn)_3C$ regions, which was applied by the integrated feature
136 within the AP Suite 6.3 software (Cameca, France). The software decomposes overlapping peaks by
137 considering the remaining unique peak(s) of the species of interest of the same charge and applies the
138 relative natural abundances to weigh the contribution of that species to the initial peak. An example for
139 this would be C_2^{1+} and C_4^{2+} in cementite. Both species exhibit peaks at 24 and 25 Da. However, C_4^{2+}
140 exhibits a unique peak at 24.5 Da as well. Considering the natural abundances of the different C_4^{2+}
141 isotopes, the contribution to the peak at 24 Da and 25 Da can be derived, which leaves the remaining
142 counts of the peaks for C_2^{1+}.

3 Results and Discussion

143 In order to answer the research questions from Sec. 1, it is essential to develop an understanding for the
144 intricacies of Fe-Mn-C pearlite formation. The main characteristic of Fe-Mn-C pearlite is the potential
145 for significant partitioning of Mn into the θ-$(Fe,Mn)_3C$ cementite while still achieving a complete
146 transformation. Hillert [12] proposed that the driving force for C diffusion in γ-(Fe,Mn,C) ahead of the
147 reaction front must be reduced in order to compensate for the orders of magnitude difference in diffusion
148 coefficients of C and Mn. A practical way shown by Hutchinson et al. [6] to ensure that such a condition
149 prevails between the two regions of interest, i.e. γ-(Fe,Mn,C) at its interface with the growing
150 θ-$(Fe,Mn)_3C$ as well as at the one with the growing α-(Fe,Mn,C), is to demand that both shall share the
151 same C activity a_C^γ. This can be elegantly applied to isothermal sections of the ternary phase diagram,
152 as depicted in Fig. 2. The compositions of austenite ahead of growing cementite and ferrite are located
153 on the same C iso-activity line in Fig. 2 (blue dots on the C iso-activity line at the intersections with the
154 metastable extensions indicated by black, dotted lines). The forming θ-$(Fe,Mn)_3C$ and α-(Fe,Mn,C) are
155 obtained from following the tie lines (blue, solid lines) connected to these γ-(Fe,Mn,C) compositions.
156 As Hutchinson et al. [6] obtained a steady-state growth of pearlite within the
157 α-(Fe,Mn,C) + θ-$(Fe,Mn)_3C$ two-phase field with constant growth rate and interphase spacing, an

158 additional boundary condition regarding the overall composition of the growing pearlite was introduced.
159 Namely, its composition must be consistent with the alloy composition. This is achieved when the
160 connecting line (blue, dashed line) between the forming θ-(Fe,Mn)$_3$C and α-(Fe,Mn,C) intersects the
161 alloy composition. Please note that this connecting line does not represent a tie line as the two growing
162 phases are not in equilibrium with each other. In what follows, this design principle is referred to as
163 steady-state, C activity-based local equilibrium condition (SCA-LE). As depicted in Fig. 2, the
164 application of the SCA-LE design indicates an enrichment of Mn in θ-(Fe,Mn)$_3$C during pearlite
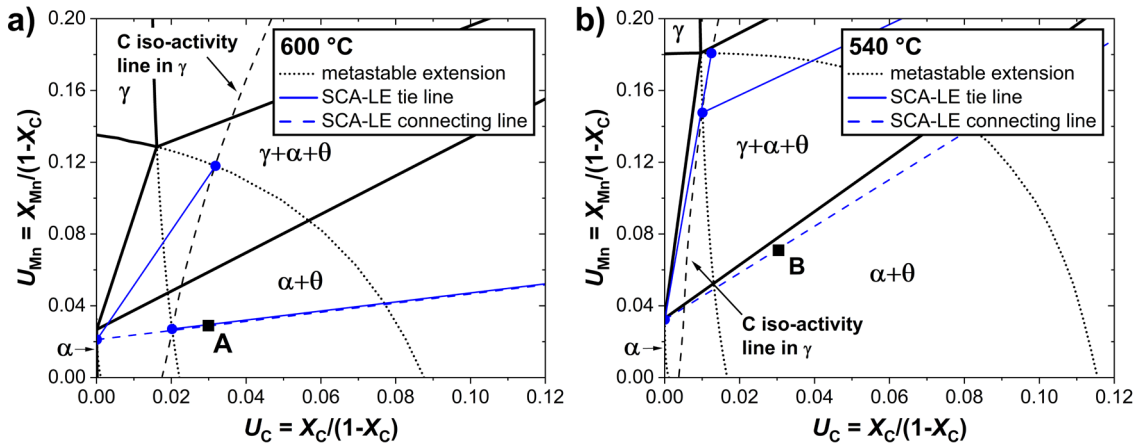165 formation even though it is being applied to the Alloys A and B outside the P-LE regime.

Fig. 2: Schematic design according to SCA-LE in isothermal sections: a) Alloy A at 600 °C and b) Alloy B at 540 °C. The illustration of the isothermal section is the same as for Fig. 1. The blue solid lines indicate tie lines while the blue dashed line is the line connecting θ-(Fe,Mn)$_3$C and α-(Fe,Mn,C) forming during steady-state pearlite growth. The predicted enrichment of Mn in θ-(Fe,Mn)$_3$C is: a) 8.0 at.% (vs. 3.0 at.% in Alloy A) and b) 35.0 at.% (vs. 6.9 at.% in Alloy B).

166 In Fig. 3, micrographs of both alloys after their respective pearlite treatment are shown, 600 °C/16 h and
167 540 °C/96 h for Alloys A and B, respectively. A complete transformation was achieved for both alloys.
168 Despite the lower transformation temperature, which is usually associated with a decrease in lamellar
169 spacing [23], Alloy B does not show a refined microstructure compared to Alloy A. With respect to the
170 pearlite morphology, a notable difference between the two alloys is obtained. Both exhibit extended
171 regions of fibrous morphology, comprising a volume fraction of (0.91 ± 0.08) and (0.32 ± 0.12) of the
172 pearlite in Alloy A and B, respectively. The volume-specific phase fraction of θ-(Fe,Mn)$_3$C, converted
173 from the area fraction under the assumption of isometry and isotropy, is (0.06 ± 0.01) for Alloy A and
174 (0.21 ± 0.02) for Alloy B. Alloy B frequently exhibits regions of increasing interface spacing towards
175 the colony boundaries, thus, at potentially late stages of the transformation before completion. These
176 regions were not included in the randomly selected micrographs to determine the volume-specific phase
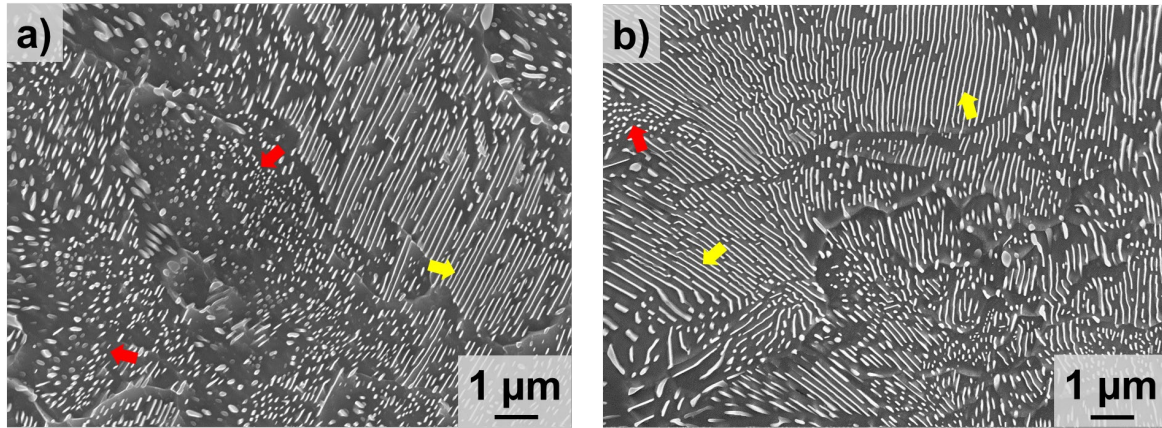177 fractions.

Fig. 3: SEM-SE micrographs (Nital etching) after completion of pearlite formation: a) Alloy A, 600 °C/16 h and b) Alloy B, 540 °C/96 h. No untransformed regions were found. θ-(Fe,Mn)$_3$C appears light, α-(Fe,Mn,C) appears dark. Lamellar morphology is indicated by yellow, fibrous by red arrows.

In order to identify the constituting phases of both alloys after the pearlite treatment, TEM-SAED patterns were recorded. Due to the large size of the pearlite colonies, TEM specimens were taken from representative regions, i.e. a fibrous colony for Alloy A and a lamellar colony for Alloy B. Both lift outs were taken in regions of near constant interface spacing with $(73 \pm 26 \text{ nm})$ and $(104 \pm 19 \text{ nm})$, respectively. Bright field micrographs as well as the TEM-SAED patterns are shown in Fig. 4. The zone axis in both Fig. 4 a) and d) is parallel to the $[100]_\theta$ direction following the lattice parameter convention, $b > a > c$ for cementite. The lift outs were chosen perpendicular to the long axes of fibers for Alloy A (Fig. 4 a)) and the lamellar plane for Alloy B (Fig. 4 c)). For both samples the constituting phases were identified as α-(Fe,Mn,C) and θ-(Fe,Mn)$_3$C by TEM-SAED patterns in Figs. 4 b) and d), respectively. Furthermore, the orientation relationship (OR) was determined. The investigated colonies of Alloy A and Alloy B both exhibit variants of the Isaichev OR $\langle 111 \rangle_\alpha || \langle 100 \rangle_\theta$, $\{1\bar{2}1\}_\alpha || \{011\}_\theta$, which is well established for pearlite [24]. Please note that Fig. 4 a) for Alloy A exhibits a twin site of the OR with a $(01\bar{1})_\theta$ habit plane instead of $(011)_\theta$ as for Fig. 4 b). The θ-(Fe,Mn)$_3$C twin variant is of compound character with the habit plane $(011)_\theta$, shear direction $[01\bar{1}]_\theta$ and shear plane $(100)_\theta$. Furthermore the twin orientation can be achieved via a rotation of the θ-(Fe,Mn)$_3$C matrix crystal around the $[100]_\theta$ direction by 111.8°. This equates to the angle between $(011)_\theta$ and $(01\bar{1})_\theta$ in a given θ-(Fe,Mn)$_3$C unit cell.

The Isaichev OR might alternatively be expressed differently by defining the habit plane according to $\{0\bar{1}1\}_\alpha || \{031\}_\theta$. This can be attributed to the very small angular mismatch (0.3°) between the sets of lattice planes involved. However, the angular mismatch becomes more apparent for high indexed spots.
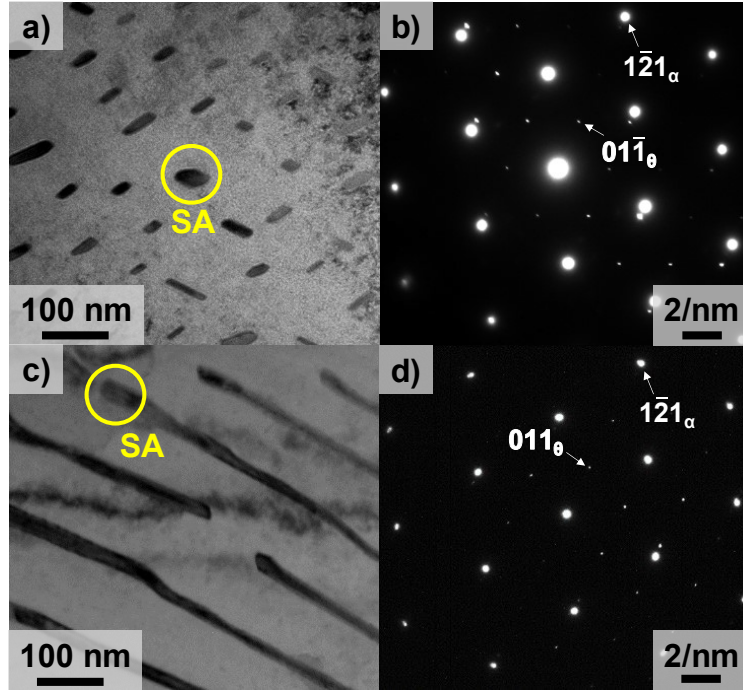
Fig. 4: TEM bright field micrographs (a),c)) and corresponding TEM-SAED patterns (b), d)) of: a), b) fibrous regions from Alloy A and c),d) lamellar region from Alloy B. The zone axes (ZA) in both b) and d) are $[111]_\alpha || [100]_\theta$.

198 Samples for APT were selected in similar fashion compared to the TEM specimens, i.e., lift out via FIB
199 in a fibrous colony for Alloy A and in a lamellar colony for Alloy B, both within regions of nearly
200 constant interface spacing. To allow for a more detailed assessment of the chemical composition, the
201 local phase fractions were determined at the lift out position. The local θ-(Fe,Mn)$_3$C volume fraction of
202 Alloy A is 0.05, while it is 0.19 for Alloy B. These values were then converted to the local molar phase
203 fractions f_m which are provided together with the values for α-(Fe,Mn,C) in Tab. 1.

Tab. 1: Compositions, C activities and molar phase fractions according to thermodynamic calculations (GE, SCA-LE), experimental (exp.) results and reconstructions. [+] denotes experimental data. [#] denotes experimental data adjusted according to the thermodynamic dataset. The other data was derived from the thermodynamic dataset.

Condition	Phase	Position	X_C	X_{Mn}	U_C	U_{Mn}	a_C^γ	f_m
Alloy A	–	–	0.029^+	0.028^+	0.030	0.029	–	–
GE	α		$1 \cdot 10^{-4}$	0.011	$1 \cdot 10^{-4}$	0.011	–	0.88
	θ		0.250	0.163	0.333	0.217	–	0.12
SCA-LE	α	γ	$1 \cdot 10^{-4}$	0.021	$1 \cdot 10^{-4}$	0.021	–	0.88
	θ	γ	0.250	0.080	0.333	0.106	–	0.12
	γ	α	0.031	0.114	0.032	0.118	0.29	–
		θ	0.020	0.027	0.020	0.027	0.29	–
Exp.	α	–	$1 \cdot 10^{-4\,+}$	0.020^+	$1 \cdot 10^{-4}$	0.020	–	0.95^+
	θ	–	0.262^+	0.218^+	0.355	0.295	–	0.05^+
Reconstr.	α	γ	$1 \cdot 10^{-4\,+}$	0.020^+	$1 \cdot 10^{-4}$	0.020	–	0.95^+
	θ	γ	$0.250^\#$	0.222^+	0.333	0.296	–	0.05^+
	γ	α	0.034	0.111	0.035	0.115	0.33	–
		Θ	0.017	0.089	0.017	0.091	0.16	–
Alloy B		–	0.029	0.069	0.030	0.071	–	–

GE	α	–	$1 \cdot 10^{-5}$	0.029	$1 \cdot 10^{-5}$	0.029	–	0.88
	θ	–	0.250	0.375	0.333	0.500	–	0.12
SCA-LE	α	γ	$1 \cdot 10^{-5}$	0.032	$1 \cdot 10^{-5}$	0.032	–	0.88
	θ	γ	0.250	0.350	0.333	0.466	–	0.12
	γ	α	0.013	0.179	0.013	0.181	0.09	–
		θ	0.010	0.147	0.010	0.148	0.09	
Exp.	α	–	$2 \cdot 10^{-4\,+}$	0.020[+]	$2 \cdot 10^{-4}$	0.020	–	0.81[+]
	θ	–	0.221[+]	0.293[+]	0.284	0.376	–	0.19[+]
Reconstr.	α	γ	$1 \cdot 10^{-4\,\#}$	0.020[+]	$1 \cdot 10^{-4}$	0.020	–	0.81[+]
	θ	γ	0.250[#]	0.282[+]	0.333	0.376	–	0.19[+]
	γ	α	0.054	0.158	0.058	0.167	0.76	–
		θ	0.011	0.106	0.011	0.107	0.14	–

204 Two reconstructed tips are depicted in Fig. 5. Both show Mn and C enrichment coinciding in the same
205 region, a θ-(Fe,Mn)$_3$C fiber (Fig. 5 a)) and lamella (Fig. 5 b)) for Alloys A and B, respectively. The
206 determined C content of θ-(Fe,Mn)$_3$C in both tips deviates from the stoichiometric expectation, which
207 may be explained by different phenomena. Possible scenarios are discussed in Ref. [25, 26]. An
208 additional aspect that could have affected the evaporation and, therefore, quantification of C is the
209 difference in θ-(Fe,Mn)$_3$C morphology. However, as the main focus of this work is the Mn partitioning,
210 this matter is not discussed further here. While Alloy A shows a Mn content of 21.8 at.% (vs. 2.8 at.%
211 in the alloy) within the θ-(Fe,Mn)$_3$C, Alloy B exhibits 29.3 at.% of Mn (vs. 6.9 at.% in the alloy). Thus,
212 Mn partitioning takes place during the pearlite reaction for both Alloys A and B, regardless of being
213 located outside the P-LE region in the isothermal sections of Fig. 1. A more detailed overview of the
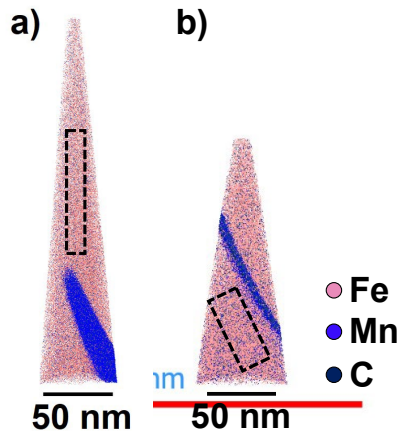214 local chemical compositions, including the C contents, are shown in Tab. 1.

Fig. 5: Reconstructed APT tip of: a) from Alloy A with a θ-(Fe,Mn)$_3$C fiber and b) Alloy B with a θ-(Fe,Mn)$_3$C lamella. Fe is represented in red, while Mn and C are represented in light and dark blue tones. The fiber and lamella are enriched in C and Mn. For α-(Fe,Mn,C), the volume that was used to determine the chemical composition is illustrated via the black boxes. For θ-(Fe,Mn)$_3$C, the analyzed volume was selected inside a Mn iso surface to avoid the effect of interphase regions.

215 The aforementioned results show that pearlite formation can lead to significant Mn partitioning even
216 when formed outside the P-LE regime. Both, the P-LE and NP-LE regime result directly from the Mn
217 partitioning boundary lines for pro-eutectoid ferrite and cementite formation, as already mentioned in
218 Sec. 1. As the boundary lines originate from the construction of the local equilibria of these two
219 reactions, they are not to be regarded as a separate concept. These boundaries strictly describe the
220 thermodynamics for partitioning between the forming α-(Fe,Mn,C) or θ-(Fe,Mn)$_3$C and the parent

221 γ-(Fe,Mn,C) by considering the LE at the reaction front as well as the rate controlling diffusion
222 processes, i.e. from the γ-(Fe,Mn,C) at the reaction front into the bulk γ-(Fe,Mn,C). As soon as the
223 predicted U_{Mn}^{α} or U_{Mn}^{θ} are equal to that of the bulk U_{Mn}^{γ} (a detailed explanation and illustration can be
224 found in the Supplementary Material and Fig. S1), Mn partitioning becomes no longer
225 thermodynamically required. The two partitioning regions therefore describe the necessity of Mn
226 partitioning based on thermodynamic considerations. Thus, if Mn partitioning shall be guaranteed by
227 thermodynamic necessity, parameters within the P-LE region should be selected. However, this does
228 not exclude the possibility that reactions outside P-LE (or even potentially within NP-LE) can exhibit
229 Mn partitioning.

230 For pearlite formation, where both partitioning boundaries are applied simultaneously, a similar line of
231 reasoning is possible. This can be attributed to the fact that during the transformation, the forming
232 α-(Fe,Mn,C) and θ-(Fe,Mn)₃C are in contact with γ-(Fe,Mn,C) at the reaction front and are therefore
233 expected to form two independent local equilibria between α-(Fe,Mn,C)/γ-(Fe,Mn,C) and
234 θ-(Fe,Mn)₃C/γ-(Fe,Mn,C), respectively. In the case of pro-eutectoid reactions, the rate controlling
235 diffusion occurs perpendicular to the reaction front. However, the pearlite formation is controlled by
236 lateral diffusion processes along or through the interfaces of the reaction front, i.e. from the γ-(Fe,Mn,C)
237 ahead of the growing α-(Fe,Mn,C) to the γ-(Fe,Mn,C) ahead of the growing θ-(Fe,Mn)₃C. If pearlite
238 formation is performed within the three-phase field, a complex partitioning behavior between
239 α-(Fe,Mn,C)/γ-(Fe,Mn,C), θ-(Fe,Mn)₃C/γ-(Fe,Mn,C) and α-(Fe,Mn,C)/θ-(Fe,Mn)₃C has to be expected,
240 with no obvious means to deduce which set of parameters might favor Mn partitioning into the
241 diminishing γ-(Fe,Mn,C) or into the growing θ-(Fe,Mn)₃C. This becomes significantly less complex,
242 when a complete reaction can be achieved. In this case, all elemental partitioning must be accommodated
243 entirely by the product phases ferrite and cementite. Hence, it is reasonable to assume that already
244 fulfilling a single partitioning criterion for pearlite formation inside the two-phase field is sufficient to
245 eventually achieve Mn partitioning between α-(Fe,Mn,C) and θ-(Fe,Mn)₃C; thus, either for
246 α-(Fe,Mn,C)/γ-(Fe,Mn,C) or θ-(Fe,Mn)₃C/γ-(Fe,Mn,C). In the present study, this is shown for the
247 practically more relevant region where the Mn partitioning criterion is fulfilled for α-(Fe,Mn,C), but not
248 for θ-(Fe,Mn)₃C formation.

249 Hutchinson et al. [6] experimentally validated the predicted pearlite composition via STEM-EDS
250 (energy-dispersive X-ray spectroscopy). In the present work, APT was chosen as it allows a significantly
251 higher degree of accuracy for both C and Mn contents [27]. To re-evaluate the viability of the SCA-LE
252 method, its main design principles will be compared to the experimental data of Alloy A and B. For the
253 comparison, it is assumed that the compositions of α-(Fe,Mn,C) and θ-(Fe,Mn)₃C, which were
254 experimentally determined post-transformation (Tab. 1), correspond to their compositions during the
255 reaction, i.e., to the composition right after the reaction front has passed the region of interest. Since the
256 pearlite treatment was terminated shortly after a complete transformation, a comparison between the LE
257 model and post-transformation experimental data is deemed viable. The APT data of the two product
258 phases allows for a reconstruction of the γ-(Fe,Mn,C)/α-(Fe,Mn,C) and γ-(Fe,Mn,C)/θ-(Fe,Mn)₃C tie
259 lines, as each composition may only be described by a single tie line. The validation will focus on
260 whether the reconstructed tie line end points for the γ-(Fe,Mn,C)/α-(Fe,Mn,C) and
261 γ-(Fe,Mn,C)/θ-(Fe,Mn)₃C interfaces share the same C iso-activity and whether the connecting line
262 between the α-(Fe,Mn,C) and θ-(Fe,Mn)₃C compositions intersects the overall alloy composition.

263 For the γ-(Fe,Mn,C)/θ-(Fe,Mn)₃C tie line reconstruction, the C content within the θ-(Fe,Mn)₃C was set
264 to 25.0 at.%. This was done via a count correction of the C ions and therefore the total amount of ions
265 that were included in the APT analysis of θ-(Fe,Mn)₃C. The resulting Mn content was then deliberately

266 equipped with a conservative uncertainty of ± 3.0 at.% to account for any inaccuracies regarding the
267 quantification of C. The α-(Fe,Mn,C) composition was not changed, however, as the determined
268 composition does not lie exactly on the respective metastable phase field extension, the reconstructed
269 γ-(Fe,Mn,C)/α-(Fe,Mn,C) tie line slightly differs in its α-(Fe,Mn,C) composition. Fig. 6 shows the
270 reconstructed tie lines as well as the connecting line for Alloys A in Fig. 6 a) and B in Fig. 6 b). The
271 compositions of all phases at the respective interfaces, as well as the C activities in γ-(Fe,Mn,C) a_C^γ are
272 appended to Tab. 1 as the reconstructed data. To further assist with the analysis, the GE condition that
273 might be achieved after an infinitely long hold time is also given in Tab. 1.
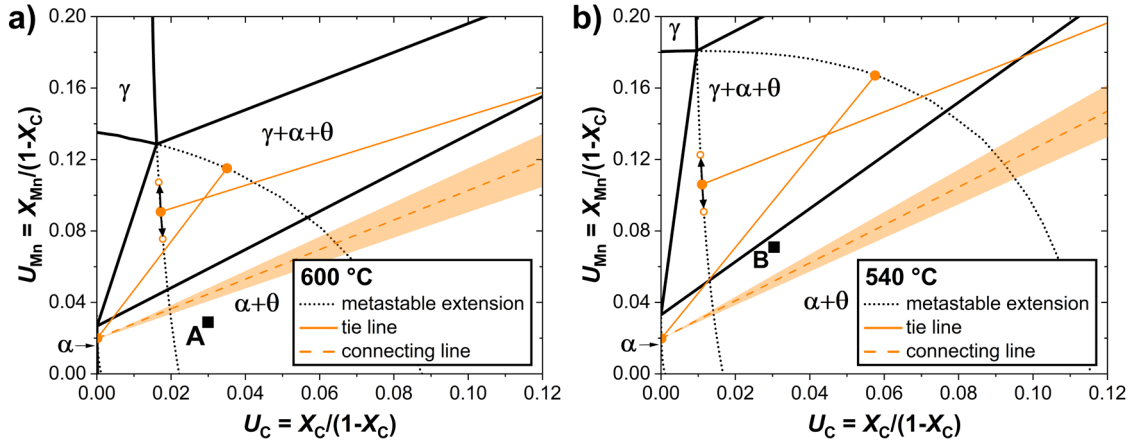
Fig. 6: Fe-Mn-C isotherms at 600 °C in a) and 540 °C in b) showing the theoretically active tie lines (orange, full), as well as the line connecting (orange, dashed) the α-(Fe,Mn,C) and θ-(Fe,Mn)₃C compositions. The applied uncertainty for the composition of θ-(Fe,Mn)₃C impacts both the position of the connecting line as well as the γ-(Fe,Mn,C)/θ-(Fe,Mn)₃C tie line. The possible positions of the connecting line are indicated by an orange box. For the endpoints of the γ-(Fe,Mn,C)/θ-(Fe,Mn)₃C tie line, the possible range is indicated by black arrows and open data points (orange). Alloy A and Alloy B both lie considerably off the connecting line.

274 Considering Tab. 1, it can be seen that the γ-(Fe,Mn,C) in front of the growing α-(Fe,Mn,C) and
275 θ-(Fe,Mn)₃C does not share the same C activity for both alloys. This remains true even when the
276 conservative uncertainty of the θ-(Fe,Mn)₃C composition is taken into account. A possible explanation
277 for these deviations could be that the pearlite composition has already significantly deviated from the
278 LE conditions during the reaction, which would make a comparison between experimental and any LE
279 data unreasonable. Assuming the SCA-LE method provides correct predictions, this would necessitate
280 that the experimental data of ferrite and cementite lie somewhere between SCA-LE and GE as the system
281 needs to change from SCA-LE to GE. However, for both alloys this is not the case. For Alloy A, SCA-
282 LE predicts the X_{Mn} of θ-(Fe,Mn)₃C as 8.0 at.%, which is lower than the GE value of 16.4 at.%. The
283 adapted experimental data of (22 ± 3) at.%, however, is significantly higher than both predictions. In
284 case of Alloy B, SCA-LE similarly predicts a lower X_{Mn} than GE, with 35.0 < 37.5 at.%, which are both
285 higher than the adapted experimental data of (28 ± 3) at.%. The deviation of the experimental data from
286 the LE conditions can therefore be considered negligible.

287 Furthermore, the connecting line between α-(Fe,Mn,C) and θ-(Fe,Mn)₃C does not intersect the alloy
288 composition for both alloys. Such a scenario is only possible if the composition of the forming pearlite
289 does not correspond to the overall composition of the alloy, i.e., the reaction does not meet steady-state
290 conditions. Hutchinson et al. [6] already hinted at and included such a possibility when introducing the
291 SCA-LE model. As the C iso-activity line, which determines the local equilibria at the reaction front in
292 SCA-LE, is not required to intersect the alloy composition, C diffusion between γ-(Fe,Mn,C) at the
293 interface and the bulk is theoretically possible (given a difference in C activity exists). Despite this, the
294 transformation follows apparent steady-state conditions for most of the duration, with a near constant

interface velocity and interface spacing [6]. This growth continues until the change in C content within the diminishing γ-(Fe,Mn,C) becomes so drastic that an abrupt change in growth is required. In Fe-Mn-C pearlite, this may be expressed by a sudden increase or decrease in the interface spacing of the θ-(Fe,Mn)$_3$C [6]. One aspect that must be mentioned in this context is that the spacing alone is insufficient to describe this phenomenon. As C solubility in α-(Fe,Mn,C) and θ-(Fe,Mn)$_3$C is either extremely small or at a stoichiometric 25 at.%, a drastic change in C content in the γ-(Fe,Mn,C) near the reaction front can only be accommodated by a shift in the product phase fractions. Additionally, an increase or decrease in interphase spacing may be observed.

For the two cases depicted in Fig. 2, SCA-LE predicts that the activities in bulk γ-(Fe,Mn,C) are higher than in the near-interface γ-(Fe,Mn,C). Thus, a diffusion flux of C towards the interface would be possible during most of the growth for both alloys, potentially depleting the bulk γ-(Fe,Mn,C) in C. In contrast, the SCA-LE reconstructions of the experimental results indicate that the C activity of γ-(Fe,Mn,C) ahead of the growing α-(Fe,Mn,C) is larger than that ahead of θ-(Fe,Mn)$_3$C, while the C activity of the bulk γ-(Fe,Mn,C) is larger than both for Alloy A and in-between the two for Alloy B. To further investigate any possible bulk diffusion during the reaction, analyzing the local chemical composition of the product pearlite is a viable method. Of interest is the deviation of both the Mn and C content between the pearlite and the bulk γ-(Fe,Mn,C), which is considered to be equal to the overall alloy composition for a large part of the reaction.

In order to determine the local composition of pearlite, both the chemical composition as well as the phase fractions of the product phases are necessary and summarized for Alloys A and B in Tab. 1. This allows for the actual composition of the pearlite to be calculated, following

$$\begin{pmatrix} X_C \\ X_{Mn} \end{pmatrix} = \begin{pmatrix} X_C^\alpha & X_C^\theta \\ X_{Mn}^\alpha & X_{Mn}^\theta \end{pmatrix} \begin{pmatrix} f_\alpha \\ f_\theta \end{pmatrix}. \tag{1}$$

Here, X_Y represents the total molar fraction of the element Y within the pearlite in the region of interest, X_Y^Z is the molar fraction of Y in phase Z and f_Z is the molar fraction of phase Z. For Alloy A, the local composition of the pearlite is X_C = 1.3 at.% and X_{Mn} = (3.0 ± 0.2) at.% (vs. 2.9 at.% C and 2.8 at.% Mn in the alloy) and for Alloy B X_C = 4.8 at.% and X_{Mn} = (7.0 ± 0.6) at.% (vs. 2.9 at.% C and 6.9 at.% Mn in the alloy). For both cases, pearlite resembles the Mn content of the bulk γ-(Fe,Mn,C) (alloy composition), but not the C content. In case of Alloy A, γ-(Fe,Mn,C) would become enriched in C during growth, while the C content in γ-(Fe,Mn,C) would have decreased in Alloy B. However, characteristic features in the microstructure suggesting such varying growth conditions were only observed in Alloy B. Here, depending on the orientation of the pearlite colonies to the surface, an increase in the lamellar spacing and a reduction in the cementite fraction was observed. In Alloy A, no features corresponding to C enrichment of γ-(Fe,Mn,C) during growth were found. The reason for this is most likely the heterogeneity of the predominantly fibrous microstructure as the longitudinal axis of the fiber must be oriented parallel to the sample surface to clearly observe changes in spacing and phase fraction during growth.

These results were not consistently predicted by considering the C activity values of the SCA-LE method. The same holds true for the experimentally reconstructed SCA-LE data. Considering the deviation of the LE model from the present experimental data, SCA-LE in its current form does not seem suitable for accurate predictions in the investigated parameter space, ranging from 3 wt.% Mn and 600 °C transformation temperature to 7 wt.% and 540 °C, respectively. In addition to the underlying diffusion problem, which revolves around simultaneous Mn and C partitioning, modelling pearlite

337 formation in the two-phase field specifically requires the consideration of two more aspects. The first
338 one is the *apparent* steady-state character of the transformation. SCA-LE was developed with the goal
339 of modelling a steady-state reaction [6]. This decision is based on the two steady-state features of the
340 reaction, namely the near constant growth rate and interface spacing (for most of the reaction). However,
341 as already mentioned by Hutchinson et al. [6] as well as in this work, while appearing as steady-state in
342 this regard, the reaction most likely exhibits constant bulk C diffusion to or away from the reaction front
343 for a large set of parameters. While SCA-LE addresses the constant volume fraction during growth by
344 the construction of the connecting line intersecting the alloy composition, the C activity difference
345 between interphase and bulk γ-(Fe,Mn,C) in most cases will violate steady-state requirements as a
346 constant diffusion flux is enforced. The second aspect revolves around the occurrence of different
347 θ-(Fe,Mn)$_3$C morphologies, which are a prominent feature in the present alloys but are rarely addressed
348 in literature. The difference in curvature of fibrous and lamellar θ-(Fe,Mn)$_3$C at the reaction front might
349 be too large to be neglected and might affect the local equilibria. In summary, a more precise LE model
350 could be developed if adequate considerations of the (quasi-)steady-state conditions and the interphase
351 curvature at the reaction front are incorporated.

352 Apart from the theoretical models to describe the Fe-Mn-C pearlite reaction, the APT results clearly
353 show a significant Mn partitioning between α-(Fe,Mn,C) and θ-(Fe,Mn)$_3$C for both alloys. In order to
354 validate if the respective Mn pattern is sufficient for the scheme introduced by Sun et al. [1], an STA
355 treatment was performed. The heat treatment was conducted at 770 °C for 150 s for both alloys and was
356 concluded via oil quenching. Micrographs after the treatment can be seen in Figs. 7 a) and b) for
357 Alloys A and B, respectively. For the given set of parameters a complete transformation to γ-(Fe,Mn,C)
358 was observed. The novel austenitic-martensitic microstructure can be easily distinguished from the
359 initial pearlite as there is a contrast inversion in both SEM-SE and SEM-BSE contrast. While in pearlite
360 the minority phase θ-(Fe,Mn)$_3$C appears bright, the minority phase of the novel microstructure,
361 γ-(Fe,Mn,C), appears dark. Both alloys largely retained their morphology when compared to the initial
362 pearlite, i.e. both still show fibrous (highlighted by red arrows in Fig. 7 a)) as well as lamellar
363 (highlighted by yellow arrows in Fig. 7) domains. However, both alloys also show regions with no
364 distinct morphology (highlighted by blue arrows in Fig. 7). After a region was transformed to
365 γ-(Fe,Mn,C), any additional hold time can be considered as a homogenization, where the Mn pattern
366 gradually dissolves. The process is expected to be fastest in regions of small lamellar spacing, as well
367 as weak Mn pattern. A significant local Mn homogenization may therefore be achieved already during
368 the transformation to γ-(Fe,Mn,C). For a given pearlitic sample, this can be partially or completely
369 avoided by choosing the STA temperature sufficiently high to allow for a fast transformation. An STA
370 temperature only slightly above A$_3$/A$_{CM}$ (C and Mn dependent lower temperature limits, at which
371 ferrite/cementite will be entirely transformed to austenite) may result in a slow transformation, which
372 allows already transformed regions to be homogenized before the microstructure is entirely austenitic.
373 Substantially homogenized regions are unable to retain the aspired morphology, as the peak Mn content
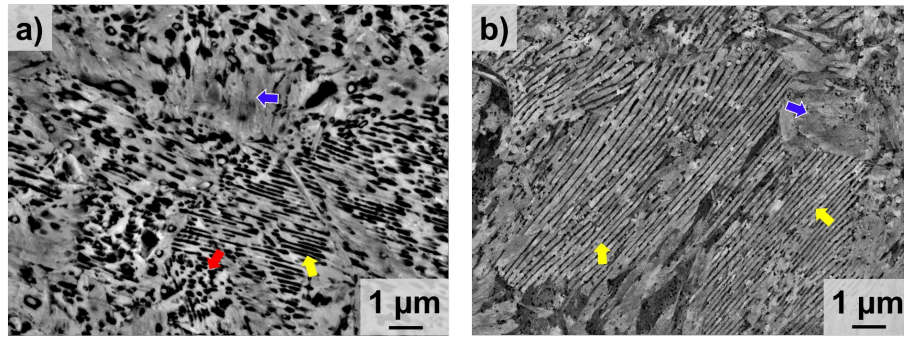374 is insufficient to stabilize γ-(Fe,Mn,C).

Fig. 7: a) and b) show micrographs of Alloys A and B using SEM-BSE (Nital etching) contrast after the STA treatment, respectively. No untransformed regions were observed for either alloy. Dark regions are austenite, while medium gray regions are martensite. Lamellar morphology is marked by yellow, the fibrous by red arrows. The blue arrows indicate regions without retained morphology.

4 Conclusions

Two model alloys were subjected to a pearlite treatment fulfilling the Mn partitioning criterion only for α-(Fe,Mn,C), but not for θ-(Fe,Mn)$_3$C and therefore outside the established P-LE and NP-LE regimes. After the pearlite formation, an STA treatment was applied. With respect to the initial research questions, the following conclusions can be drawn:

- Even at low transformation temperatures and high Mn contents, a complete pearlite transformation is achieved with α-(Fe,Mn,C) and θ-(Fe,Mn)$_3$C being the only constituting phases in the pearlite.
- Pearlite formation in the regime where the Mn partitioning condition is fulfilled only for α-(Fe,Mn,C) (and not for θ-(Fe,Mn)$_3$C) still results in considerable Mn partitioning, indicating that partitioning occurs in a wider range of Mn and C contents as well as transformation temperatures than previously assessed in literature.
- It is likely that the low Mn equilibrium solubility of α-(Fe,Mn,C) is the decisive factor for the degree of partitioning between the two product phases. Thus, if the overall Mn content exceeds the solubility limit, noticeable Mn partitioning can be expected. However, if the C content and therefore the θ-(Fe,Mn)$_3$C fraction is high, the degree of Mn partitioning might diminish.
- The chemical Mn pattern in both alloys is sufficiently strong to achieve the anticipated austenitic-martensitic microstructure via STA from such pearlite.
- The detailed analysis of experimental APT data on two Fe-Mn-C alloys, one with a low and one with a high Mn content, suggests that the reaction cannot be described using the SCA-LE method under the above conditions. The reconstructed tie lines do not share a common C iso-activity in γ-(Fe,Mn,C). Furthermore, the reaction does not follow conventional steady-state conditions, as already indicated in Ref. [6]. Despite a quasi-steady-state growth for most of the reaction, the pearlite inherits the overall alloy composition only with respect to the Mn content. The C content may vary during growth, enabling a significant deviation of the phase fractions within the quasi-steady-state regions compared to the predicted GE values.

Data Availability Statement

Declaration of Competing Interest

Acknowledgments

References

[1] Sun, W.W. et al.: Advanced high strength steel (AHSS) development through chemical patterning of austenite. *Scripta Materialia*, **146** (5), 2018, p. 60–63.

[2] Li, S. et al.: Study of partition to non-partition transition of austenite growth along pearlite lamellae in near-eutectoid Fe-C-Mn alloy. *Acta Materialia*, **177**, 2019, p. 198–208.

[3] An, X.L. et al.: The role of retained austenite on the stress-strain behaviour of chemically patterned steels. *Materials Science and Engineering: A*, **831**, 2022, p. 142286.

[4] Yang, D. et al.: Mn Heterogeneity and Ductility Improvement Realized by Slow Heating Mn-Partitioned Pearlite. *Met. Mater. Int.*, **30** (2), 2024, p. 393–402.

[5] Yang, D. et al.: The abnormal carbon redistribution in lath martensite during tempering in Mn-patterned steels. *Materials Characterization*, **210**, 2024, p. 113841.

[6] Hutchinson, C.R. et al.: The growth of partitioned pearlite in Fe–C–Mn steels. *Acta Materialia*, **52** (12), 2004, p. 3565–3585.

[7] Coates, D.E.: Diffusional growth limitation and hardenability. *Metall Trans*, **4** (10), 1973, p. 2313–2325.

[8] Hillert, M.: *Phase Equilibria, Phase Diagrams and Phase Transformations: Their Thermodynamic Basis*. In: Phase Equilibria, Phase Diagrams and Phase Transformations: Their Thermodynamic Basis. Cambridge: Cambridge University Press, 2007, p. 358–366.

[9] Benz, R. et al.: Thermodynamics of the solid phases in the system Fe−Mn−C. *Metall Trans*, **4** (8), 1973, p. 1975–1986.

[10] Shen, Y.Z. et al.: M5C2 Carbides in a High-Chromium Ferritic/Martensitic Steel. *Metall Mater Trans A*, **45** (7), 2014, p. 2950–2962.

[11] Cheng, W.-C. et al.: On the Eutectoid Reaction in a Quaternary Fe-C-Mn-Al Alloy: Austenite → Ferrite + Kappa-Carbide + M23C6 Carbide. *Metall Mater Trans A*, **45** (3), 2014, p. 1199–1216.

[12] Hillert, M.: Swedish Institute for Metal Research, 1953.

[13] Eckel, J.F., Krivobok, V.N.: Alloys of iron, manganese and carbon-part VIII. *Trans. Am. Soc. St. Tr.*, **21**, 1933, p. 846–864.

440 [14] Gensamer, M.: Alloys of iron and manganese-part XII. *Trans. Am. Soc. St. Tr.*, **21**, 1933, p. 1028–
441   1034.

442 [15] Hillert, M., Waldenström, M.: A thermodynamic analysis of the Fe-Mn-C system. *Metall Trans A*,
443   **8** (1), 1977, p. 5–13.

444 [16] Stefanescu, D., Katz, S.: *Thermodynamic Properties of Iron-Base Alloys*. In: Casting (Editors: S.
445   Viswanathan et al.). Ohio: ASM International, 2008, p. 41–55.

446 [17] Bain, E.C. et al.: The equilibrium diagram of iron-manganese-carbon alloys of commercial purity.
447   *Tran. Am. Inst. Min. Metall. Eng.*, (100), 1932, p. 228–256.

448 [18] Tofaute, W., Linden, K.: Die Umwandlung im festen Zustande bei Manganstählen mit Gehalten bis
449   1,2% C und 17% Mn. *Archiv für das Eisenhüttenwesen*, **10** (11), 1937, p. 515–524.

450 [19] Vogel, R., Döring, W.: Das System Eisen-Zementit-Mangankarbid-Mangan. *Archiv für das*
451   *Eisenhüttenwesen*, **9** (5), 1935, p. 247–252.

452 [20] Walters, F.M., Wells, C.: Alloys of iron and manganese-part XIII. *Trans. ASM*, **23** (3), 1935, p.
453   727–750.

454 [21] Walters, F.M., Wells, C.: Alloys of iron, manganese and carbon-part XIV. *Trans. ASM*, **23** (3),
455   1935, p. 751–760.

456 [22] Münch, M., Kauffmann, A.: Matlab code to 'Assessment of the compositional requirements to form
457   Fe-Mn-C austenite-martensite composites'. 2025.

458 [23] Mehl, R.F., Hagel, W.C.: The austenite: Pearlite reaction. *Progress in Metal Physics*, **6**, 1956, p.
459   74–134.

460 [24] Zhou, D.S., Shiflet, G.J.: Ferrite: Cementite crystallography in pearlite. *Metall Trans A*, **23** (4),
461   1992, p. 1259–1269.

462 [25] Peng, Z. et al.: Unraveling the Metastability of Cn2+ (n = 2–4) Clusters. *J. Phys. Chem. Lett.*, **10**
463   (3), 2019, p. 581–588.

464 [26] Takahashi, J. et al.: Study on Quantitative Analysis of Carbon and Nitrogen in Stoichiometric θ-
465   Fe3C and γ′-Fe4N by Atom Probe Tomography. *Microscopy and Microanalysis*, **26** (2), 2020, p.
466   185–193.

467 [27] Gault, B. et al.: Atom probe tomography. *Nat Rev Methods Primers*, **1** (1), 2021, p. 1–30.

468